ELSEVIER

Journal of Materials Processing Technology 89–90 (1999) 331–338

Journal of Materials Processing Technology

An elasto-plastic finite-element analysis of the metal sheet redrawing process

You-Min Huang [a,*], Ching-Lun Li [b]

[a] *Department of Mechanical Engineering, National Taiwan University of Science and Technology, 43 Keelung Road, Section 4, Taipei 10672, Taiwan, ROC*

[b] *Department of Mechanical Engineering, Tamkang University, 151 Ying-chuan Road, Tamsui, Taipei Hsien 25137, Taiwan, ROC*

Received 22 September 1998

Abstract

A methodology for formulating an elasto-plastic finite-element model, based on an updated Lagrangian formulation and the Prandtl–Reuss flow rule, was developed to simulate the redrawing process of axisymmetric sheet metal. An extended r_{min} algorithm is proposed to formulate the boundary conditions, such as nodal penetration and separation, alteration of the sliding direction of friction, linearization of strains increments and rotational increments and altered elasto-plastic state of the material. A modified Coulomb's friction law is introduced to describe the alternation between the sliding state and sticking state of faction at the contact interface. The corresponding stiffness equations and solution algorithms are introduced. According to the developed finite-element model, the redrawing process of sheet metal is simulated. Simulation results, such as: (i) the whole deformation history; (ii) the entire loading process history; and (iii) thickness of the workpieces, etc. can be obtained. The simulation clearly demonstrates the efficiency of the model to simulate the redrawing process of sheet metal. This paper has provided a greater understanding of the redrawing process which can lead to improvements in the manufacturing process and in the design of tools.

Keywords: Redrawing process; Elasto-plastic; Finite-element

1. Introduction

The redrawing process has been used for the production of deeper and narrower cups. If the first drawing operation cannot produce a cup that is deep or tapered enough, because of encountering a limiting drawing ratio, redrawing has to be employed. If the first redraw still can not produce the deeper cup, a second redraw is employed, and so on.

Early in the 1940s, Swift dedicated his research to redrawing; afterwards, Swift and Chung [1] investigated experiments on cylindrical cups redrawing. Nakamura and Nakagawa [2] proposed the application of hydraulic counter pressure and its radial pushing to reverse the redrawing process to improve the limiting drawing ratio. Parsa et al. [3] used the results of the rigid–plastic finite-element simulation to show that the success or failure of the redrawing process depends not only on the redrawing ratio but also on the work-hardening characteristics of the blank material, the first stage drawing ratio, the tool shape and the interstage annealing on the limiting redrawing ratio. Yang et al. [4] proposed a separated radial pressure assisted by a hydromechanical deep drawing process to increase the formability and productivity, which was confirmed through an experiment and a finite-element analysis. Lu and Huang [5] proposed the most adequate scheme of the stiffness matrix to solve the elasto-plastic finite-element analysis of the axisymmetric cylindrical cup drawing and redrawing process.

The constant strain triangular (CST) element and the quadrilateral element are often used in sheet metal forming problems. The full integration (FI) scheme is normally used to construct the stiffness matrix on the finite element. However, the Fl scheme of the quadrilateral element is known to form an elastic incompressible state [6,7], hence the reduced integration (RI) scheme is

* Corresponding author.
E-mail address: ymhuang@mail.ntust.edu.tw (Y.-M. Huang)

0924-0136/99/$ - see front matter
PII: S0924-0136(99)00014-X

proposed to deal with the plate bending problem. The use of the RI scheme removes the over-constraint problem, but introduces spurious zero-energy modes, which can result in the 'hourglass' phenomenon in the deformation of a thin plate [8]. A compromise known as selective reduced integration (SRI) can be used, in which RI is used to calculate the transverse shear stiffness, whereas FI is used to treat the remaining stiffness. In order to prevent the 'hourglass' phenomenon and eliminate the rank deficiency of the one-point integration scheme, Belytschko et al. [9] suggested a stabilization matrix (SM) in the four-node Mindlin plate element; and Liu et al. [10] proposed incorporating the stabilization matrix into the usual one-point integration stiffness matrix.

In this paper, the elasto-plastic finite-element based on the updated Lagrangian formulation theory and the Prandtl–Reuss flow rule has been used to simulate the process of cylindrical cup drawing and redrawing. An extended $r_{\min}$ algorithm [11] is incorporated into the computer code to determine the increment of the punch displacement. According to the results of experiment and numerical simulation, the stabilization matrix scheme presented in this paper shows good agreement with experiment in the relationship of punch load versus punch travel, and thickness variation of the workpiece.

2. Basic theory

2.1. Equilibrium equation

In applying incremental deformation toward the metal-forming process, the updated Lagrangian formulation (ULF) can be adopted flexibly to describe the incremental characteristics of the plastic law. In the ULF, the current configuration at each deformation stage is used as the reference state to evaluate the deformation in a very small time interval Δt so that the first-order theory is consistent with the accuracy requirement.

The virtual work-rate equation of the updated Lagrangian equation is written as [11]

$$\int_V \left(\overset{*}{\tau} - 2\sigma\,\dot{\epsilon} \right) \delta\,\dot{\epsilon}\,\mathrm{d}V + \int_V \sigma\,\dot{\boldsymbol{L}}\,\delta\,\dot{\boldsymbol{L}}\,\mathrm{d}V = \int_{S_\mathrm{f}} \dot{\bar{\boldsymbol{t}}}\,\delta\,\boldsymbol{v}\,\mathrm{d}S \quad (1)$$

where is the Jaumann rate of Kirchhoff stress; σ is the true stress; $\dot{\epsilon}$ and $\dot{\boldsymbol{L}}$ are the strain rate and velocity gradient, respectively; V and S_f are the material volume and the surface on which the traction is prescribed, respectively; $\boldsymbol{v}$ is the velocity; and $\dot{\bar{\boldsymbol{t}}}$ denotes the rate of nominal traction. Assuming that the distribution of the velocity $\boldsymbol{v}$ in an element is:

$$\boldsymbol{v} = \boldsymbol{N}\dot{\boldsymbol{d}} \quad (2)$$

where $\boldsymbol{N}$ is the shape function and $\dot{\boldsymbol{d}}$ indicates the nodal velocity. The strain rate and velocity gradient are written as:

$$\dot{\epsilon} = \mathbf{B}\,\dot{\boldsymbol{d}} \quad (3)$$

$$\dot{\boldsymbol{L}} = \mathbf{E}\,\dot{\boldsymbol{d}} \quad (4)$$

where $\mathbf{B}$ and $\mathbf{E}$ indicate the strain rate–velocity matrix and the velocity gradient–velocity matrix, respectively. By substituting (Eqs. (3) and (4) into Eq. (1)), the elemental stiffness matrix equation is:

$$\mathbf{K}\dot{\boldsymbol{d}} = \dot{\boldsymbol{F}} \quad (5)$$

in which:

$$\mathbf{K} = \int_{V\langle e\rangle} \mathbf{B}^T (\mathbf{D}_{\mathrm{ep}} - \mathbf{Q})\mathbf{B}\,dV + \int_{V\langle e\rangle} \mathbf{E}^T\mathbf{G}\,\mathbf{E}\,dV$$

$$\dot{\boldsymbol{F}} = \int_{S\langle e\rangle} \mathbf{N}^T\,\dot{\bar{\boldsymbol{t}}}\,dS$$

In these equations, $\mathbf{K}$ is the tangential stiffness matrix, $\mathbf{D}_{\mathrm{ep}}$ is the elemental elasto-plastic constitutive matrix, $\dot{\boldsymbol{F}}$ is the nominal force rate, $\mathbf{Q}$ and $\mathbf{G}$ are defined as stress correction matrices due to the current stress states at each deformation stage, and V and S are the domains of volume and surface of the element, respectively.

2.2. Full integration (FI)

Full integration is always to be used for a displacement-based or mixed finite-element formulation. For the 4-node quadrilateral element, Eq. (5) can be integrated by evaluating the elemental stiffness matrix at all four Gauss points.

2.3. Reduced integration (RI)

Using this integration scheme, the stiffness matrix is evaluated at the central point of the element. In most cases the reduced integration scheme gives a zero energy mode and this is the reason why it should be avoided in ordinary simulation.

2.4. Selective reduced integration (SRI)

In the selective reduced integration scheme, the bending term is integrated with the full integration rule, whereas the shear term is integrated by the one-point Gaussian quadrature that is the reduced integration for the 4-node quadrilateral element.

2.5. Stabilization matrix (SM)

As the reduced one-point integration scheme for the 4-node quadrilateral element often causes a serious distortion of elements known as the hourglass effect, Liu et al [10] proposed adding an element stabilized

matrix $\mathbf{K}^s$ to the one-point integration element stiffness matrix $\mathbf{K}^1$ to form the element stiffness matrix $\mathbf{K}$ in Eq. (5). Hence, the resulting elemental stiffness matrix becomes:

$$\mathbf{K} = \mathbf{K}^1 + \mathbf{K}^s \tag{6}$$

Superscript 1 denotes one-point integration in the element. Evaluation of the matrices $\mathbf{K}^1$ and $\mathbf{K}^s$ is provided in this section. Initially, the strain rate and velocity gradient are approximated by Taylor's equation at the origin of natural coordinates ξ and η as follows:

$$\dot{\varepsilon}(\xi, \eta) = \mathbf{B}_i(0)\dot{\boldsymbol{d}}_i + \mathbf{B}_{i,\,\xi}(0)\dot{\boldsymbol{d}}_i\,\xi + \mathbf{B}_{i,\,\eta}(0)\dot{\boldsymbol{d}}_i\,\eta \tag{7}$$

$$\dot{\boldsymbol{L}}(\xi, \eta) = \mathbf{E}_i(0)\dot{\boldsymbol{d}}_i + \mathbf{E}_{i,\,\xi}(0)\dot{\boldsymbol{d}}_i\,\xi + \mathbf{E}_{i,\,\eta}(0)\dot{\boldsymbol{d}}_i\,\eta \tag{8}$$

where i is summed from 1 to the number of nodes per element, for a quadrilateral element this number being 4. The comma indicates partial differentiation. (0) denotes the evaluation calculated at $(\xi,\ \eta) = (0,\ 0)$. By substituting strain rate and velocity gradient Eqs. (7) and (8) into Eq. (1), the submatrices $\mathbf{K}^1_{ab}$ and $\mathbf{K}^s_{ab}$ for nodes a and b in the element are obtained by calculating the integral of Eq. (5) at the origin of the natural coordinates:

$$\mathbf{K}^1_{ab} = V\,\mathbf{B}^T_a(0)(\mathbf{D}_{\mathrm{ep}} - \mathbf{Q})\mathbf{B}_b(0) + V\,\mathbf{E}^T_a(0)\mathbf{G}\,\mathbf{E}_b(0) \tag{9}$$

and:

$$\mathbf{K}^s_{ab} = \frac{1}{3}V\,\mathbf{B}^T_{a,\,\xi}(0)(\mathbf{D}_{\mathrm{ep}} - \mathbf{Q})\mathbf{B}_{b,\,\xi}(0)$$

$$+\frac{1}{3}V\,\mathbf{B}^T_{a,\,\eta}(0)(\mathbf{D}_{\mathrm{ep}} - \mathbf{Q})\mathbf{B}_{b,\,\eta}(0)$$

$$+\frac{1}{3}V\,\mathbf{E}^T_{a,\,\xi}(0)\mathbf{G}\,\mathbf{E}_{b,\,\xi}(0) + \frac{1}{3}V\,\mathbf{E}^T_{a,\,\eta}(0)\mathbf{G}\,\mathbf{E}_{b,\,\eta}(0) \tag{10}$$

In a nearly incompressible medium, the plastic deformation is due primarily to the deviatoric part of $\mathbf{B}_i$ and $\mathbf{E}_i$, hence, the stabilized matrix $\mathbf{K}^s_{ab}$ can be redefined as follows:

$$\mathbf{K}^s_{ab} = \frac{1}{3}V\,\mathbf{B}^{\mathrm{dev}}_{a,\,\xi}(0)^T(\mathbf{D}_{\mathrm{ep}} - \mathbf{Q})\mathbf{B}^{\mathrm{dev}}_{b,\,\xi}(0)$$

$$+\frac{1}{3}V\,\mathbf{B}^{\mathrm{dev}}_{a,\,\eta}(0)^T(\mathbf{D}_{\mathrm{ep}} - \mathbf{Q})\mathbf{B}^{\mathrm{dev}}_{b,\,\eta}(0)$$

$$+\frac{1}{3}V\,\mathbf{E}^{\mathrm{dev}}_{a,\,\xi}(0)^T\mathbf{G}\,\mathbf{E}^{\mathrm{dev}}_{b,\,\xi}(0) + \frac{1}{3}V\,\mathbf{E}^{\mathrm{dev}}_{a,\,\eta}(0)^T\mathbf{G}\,\mathbf{E}^{\mathrm{dev}}_{b,\,\eta}(0) \tag{11}$$

In axisymmetric problems, the computations of $\mathbf{K}^1_{ab}$ require the evaluations of $\mathbf{B}_i(0)$ and $\mathbf{E}_i(0)$. The explicit form of $\mathbf{B}_i(0)$ for the 4-node quadrilateral element can be written as:

$$\mathbf{B}_i(0) = \begin{bmatrix} b_{1i} & 0 \\ 0 & b_{2i} \\ b_{2i} & b_{1i} \\ \dfrac{N_i}{r} & 0 \end{bmatrix}, \quad i = 1,\ldots,4 \tag{12}$$

where:

$$\boldsymbol{b}_1 = \{b_{1i}\} = \frac{1}{24}[z_{24,}\, z_{31,}\, z_{42,}\, z_{13}]^T \tag{13}$$

$$b_2 = \{b_{2i}\} = \frac{1}{24}[r_{42,}\, r_{13,}\, r_{24,}\, r_{31}]^T \tag{14}$$

$$r_{IJ} = r_I - r_j;\ z_{IJ} = z_I - z_J \tag{15}$$

and

$$A = \frac{1}{2}(r_{31}z_{42} + r_{24}z_{31}) \tag{16}$$

where A is the area of the quadrilateral element. A similar procedure must be performed to obtain the explicit form of $\mathbf{E}_i(0)$.

The $\mathbf{K}^s_{ab}$ computations have to determine $\mathbf{B}_{i,\,\xi}$, $\mathbf{B}_{i,\,\eta}$, $\mathbf{E}_{i,\,\xi}$, $\mathbf{E}_{i,\,\eta}$ at the origin, namely $(\xi,\ \eta) = (0,\ 0)$. Five vectors $\boldsymbol{r}$, $\boldsymbol{z}$, ξ, η and $\boldsymbol{h}$ are denoted as:

$$\boldsymbol{r} = [r^1,\ r^2,\ r^3,\ r^4]^T \tag{17}$$

$$\boldsymbol{z} = [z^1,\ z^2,\ z^3,\ z4]^T \tag{18}$$

$$\xi = [-1,\ 1,\ 1,\ -1]^T \tag{19}$$

$$\eta = [-1,\ -1,\ 1,\ 1]^T \tag{20}$$

and:

$$\boldsymbol{h} = [1,\ -1,\ 1,\ -1]^T \tag{21}$$

where ξ_i and η_i are the components of the natural coordinates for the ith node of the quadrilateral element, r_i and z_i are the components for the ith node in the global coordinate, and $\boldsymbol{h}$ is the hourglass vector [10]. After some computations and arrangements, the explicit forms of $\mathbf{B}_{i,\,\xi}(0)$ and $\mathbf{B}_{i,\eta}(0)$ are found to be:

$$\mathbf{B}^{\mathrm{dev}}_{i,\,\xi}(0) = \begin{bmatrix} \dfrac{2}{3}b_{1i,\,\xi} & -\dfrac{1}{3}b_{2i,\,\xi} \\ -\dfrac{1}{3}b_{1i,\,\xi} & \dfrac{2}{3}b_{2i,\,\xi} \\ b_{2i,\,\xi} & b_{1i,\,\xi} \\ -\dfrac{1}{3}b_{1i,\,\xi} & -\dfrac{1}{3}b_{2i,\,\xi} \end{bmatrix}, \quad i = 1,\ldots,4 \tag{22}$$

and:

$$\mathbf{B}_{i,\eta}^{\mathrm{dev}}(0)=\begin{bmatrix} \frac{2}{3}b_{1i,\eta} & -\frac{1}{3}b_{2i,\eta} \\ -\frac{1}{3}b_{1i,\eta} & \frac{2}{3}b_{2i,\eta} \\ b_{2i,\eta} & b_{1i,\eta} \\ -\frac{1}{3}b_{1i,\eta} & -\frac{1}{3}b_{2i,\eta} \end{bmatrix}, \quad i=1,\ldots,4 \tag{23}$$

where:

$$\boldsymbol{b}_{1,\xi}=\{b_{1i,\xi}\}=-\frac{(\xi^T\boldsymbol{z})}{4A}[\gamma_1,\gamma_2,\gamma_3,\gamma_4]^T \tag{24}$$

$$\boldsymbol{b}_{2,\xi}=\{b_{2i,\xi}\}=\frac{(\xi^T\boldsymbol{r})}{4A}[\gamma_1,\gamma_2,\gamma_3,\gamma_4]^T \tag{25}$$

$$\boldsymbol{b}_{1,\eta}=\{b_{1i,\eta}\}=\frac{(\eta^T\boldsymbol{z})}{4A}[\gamma_1,\gamma_2,\gamma_3,\gamma_4]^T \tag{26}$$

and:

$$\boldsymbol{b}_{2,\eta}=\{b_{2i,\eta}\}=-\frac{(\eta^T\boldsymbol{r})}{4A}[\gamma_1,\gamma_2,\gamma_3,\gamma_4]^T \tag{27}$$

In these equations, γ vector is related to $\boldsymbol{b}_1$ and $\boldsymbol{b}_2$ by $\gamma=\boldsymbol{h}-(\boldsymbol{h}^T\boldsymbol{r})\boldsymbol{b}_1-(\boldsymbol{h}^T\boldsymbol{z})\boldsymbol{b}_2$

Similarly, the explicit forms of $\mathbf{E}_{i,\xi}^{\mathrm{dev}}(0)$, $\mathbf{E}_{i,\eta}^{\mathrm{dev}}(0)$ can be computed in the same procedure. By using the explicit forms of $\mathbf{B}_i(0)$, $\mathbf{E}_i(0)$, $\mathbf{B}_{i,\xi}^{\mathrm{dev}}(0)$, $\mathbf{B}_{i,\eta}^{\mathrm{dev}}(0)$, $\mathbf{E}_{i,\xi}^{\mathrm{dev}}(0)$ and $\mathbf{E}_{i,\eta}^{\mathrm{dev}}(0)$, the explicit $\mathbf{K}_{ab}^{\mathrm{l}}$ and $\mathbf{K}_{ab}^{\mathrm{s}}$ can be evaluated.

3. Experiment and FEM analysis

3.1. Experimental work

To verify the development of the computer code, experiments were conducted to examine the process of cylindrical cup drawing and redrawing. The experimental equipment involved a 500 kN hydraulic press with two cylinders. The press was PLC-controlled and mounted with transducers for measuring the position and force on each cylinder. The PLC-controller was linked to data acquisition equipment enabling the press to be computer controlled.

Lubrication of the workpieces plays an important role in the drawing and redrawing process. The usage of lubricant is not only to diminish the friction between the sheet and die, but also to increase the life of the die. In the present experiment, the lubricant adopted was zinc stearate. The experimental procedure was performed as follows:

(1) Use a pressing mold to cut the blanks, the diameters of which were equal to 140.0 mm; (2) assemble the die sets on the hydraulic press; (3) spray a thin film of zinc stearate onto both sides of the blank; (4) use a three-point adjustment to center the blank on the die; (5) put the spacer ring around the blank. Next, set the blankholder force to 50 kN and press on the spacer ring; (6) select a reasonable velocity (1.4 mm s^{-1}) for the punch to draw the blank into the die; (7) record the relationship of punch load and punch travel by the data acquisition equipment; (8) repeat the steps 1–7 for the various blanks; (9) cut the workpiece along the central generatrix with a CNC wire-cutting machine; (10) stick a paper-meter along the central generatrix on the workpiece. Then, use a sharp-point micrometer to measure thickness along the central generatrix.

3.2. FEM analysis

The elasto-plastic finite-element with the updated Lagrangian formulation is used to simulate the cylindrical cup drawing and redrawing processes in this study. The analyses of cup drawing and redrawing processes are based on axisymmetric considerations. Only the right-half portion of the tools and workpiece are modeled in simulations. An auto-mesh program is used to generate the finite-element. Fig. 1 shows the tools' dimensions and the initial dimension of the blank and the finite-element mesh in the drawing process. Fig. 2 shows the tools' dimensions in the redrawing process. The sheet was meshed as one layer and 150 columns for the constant strain triangular element, and three layers and 150 columns for the quadrilateral element. The element and node number used in simulations for different element types are shown in Table 1.

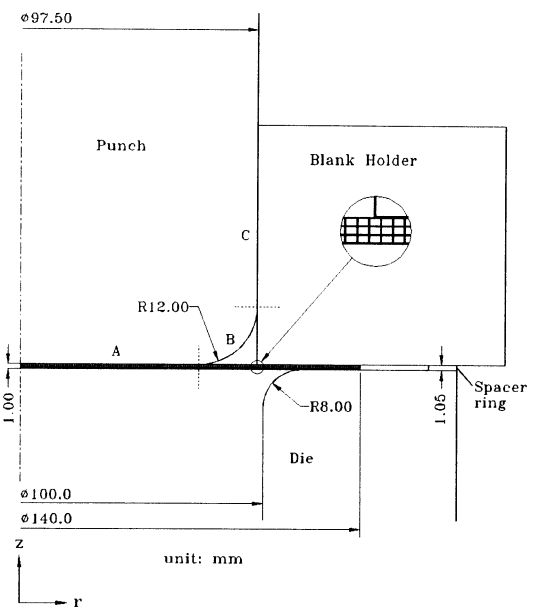

Fig. 1. Tools' dimensions and finite-element mesh of the blank for the cylindrical cup drawing process.

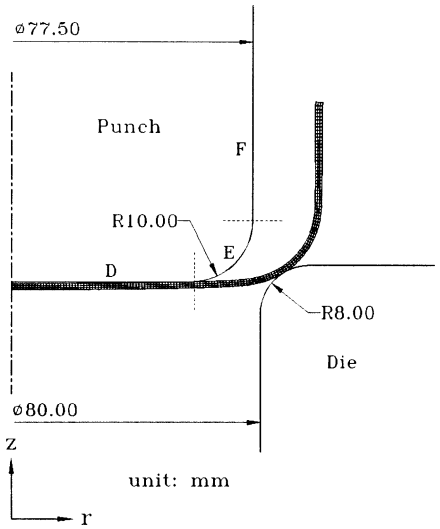

Fig. 2. Tools' dimensions for the cylindrical cup redrawing process.

Global coordinates (r, z) are used to describe factors such as nodal force, nodal displacement, element stress, and element strain. The generalized $r_{\min}$ strategy [12] is used to determine the actual punch displacement in each stage. This generalized $r_{\min}$ strategy is used to determine the minimum increment of punch travel from the following considerations: (1) a finite element cannot change state from elastic to plastic and vice versa; (2) the largest absolute value of the incremental principal strains attains a limiting value of $\Delta\varepsilon_{\max} = 0.002$; (3) the largest absolute value of the incremental rotations attains a limiting value of $\Delta\theta_{\max} = 0.5°$; (4) a free node will not come into contact; (5) a contacting node will not get free; (6) a sticking node will not slide; (7) a sliding node will not stick. The Coulomb friction law is adopted to treat the frictional effect between the tools and workpiece. All calculations were performed on a DEC Alpha $200_{4/233}$ workstation. The material used in the experiment was JIS G3141 SPCEN-SD (DDQ) low-carbon steel. The material properties and the stress-strain relationship were: blank thickness $t = 1.00$ mm; stress–strain relation $\bar{\sigma} = 516.54(0.00639 + \bar{\varepsilon}_p)^{0.232}$ MPa; and yield stress $\sigma_y = 160.00$ MPa. The values of Poisson's ratio and Young's modulus for the material were $v = 0.3$ and $E = 2.1 \times 10^5$ MPa, respectively.

Table 1
Element and node number used in simulations

Element type	Node number	Element number
Constant strain triangular	452	600
Quadrilateral	604	450

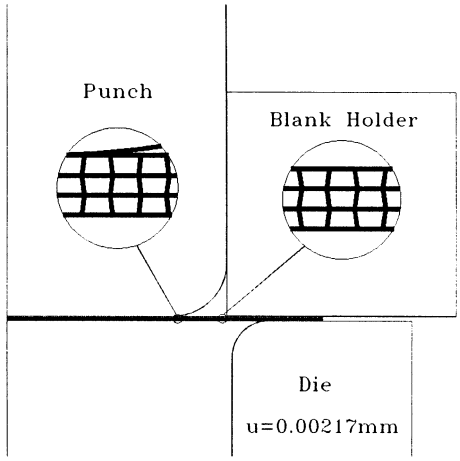

Fig. 3. 'Hourglass' effect in the reduced integration scheme.

4. Results and discussion

Both drawing and redrawing processes were used to compare with the experimental results to verify the computation code.

4.1. 'Hourglass' mode in RI scheme

To demonstrate the occurrence of the 'hourglass' phenomenon, a simulation without the stabilization matrices was executed by a one-point reduced integration scheme. Fig. 3 depicts the 'hourglass' mode when the punch travel reaches 0.00217 mm. This figure clearly indicates that the 'hourglass' mode occurred in many elements. This is due to the elements being subjected to the bending effect caused by the constraint of the die and the punch head, in the initial deformation stage.

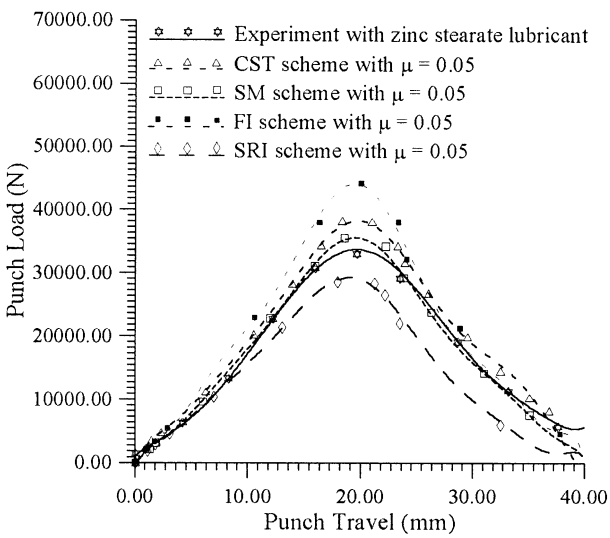

Fig. 4. Comparison of punch load for different integration schemes and experiment in the drawing process.

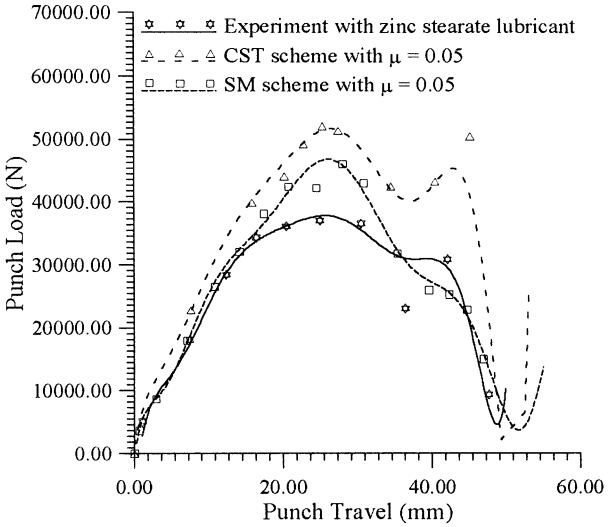

Fig. 5. Comparison of punch load for different schemes and experiment in the redrawing process.

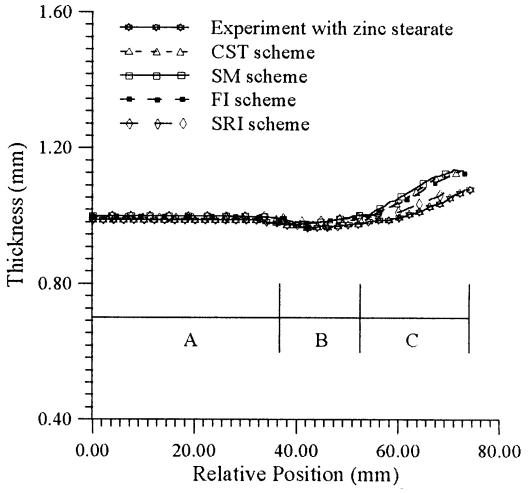

Fig. 6. Comparison of thickness for different integration schemes and experiment in the drawing process.

4.2. Comparison of the punch load in drawing and in redrawing

Fig. 4 shows a comparison between experiment and simulations for punch load versus punch travel in the drawing process, using zinc stearate lubricant for the blank diameter of $\varphi = 140.0$ mm, to provide a friction coefficient of $\mu = 0.05$. It is noted that the load of the SRI scheme is obviously lower than the load of the experiment and other schemes, and the load of the FI scheme is obviously larger than the load of other schemes and the experiment.

Fig. 5 shows a comparison between experiment and simulations of the CST scheme and the SM scheme for punch load versus punch travel in the redrawing process. The load of the CST scheme is obviously larger than that for the SM scheme and that for experiment.

4.3. CPU time in simulation

For purposes of the FEM analysis, it was necessary to use the 'sufficiently accurate' rule. Hence the determination that the FEM meshed-elements does not only permit convergence but also saves CPU time was of interest in the present investigation. Table 2 illustrates the relation of CPU time versus venous integration schemes. The CPU times to simulate the drawing and redrawing process were less for the SM scheme and the CST scheme than for the FI scheme and the SRI scheme.

4.4. Comparison of the sheet thickness

An NC wire-cutting machine was used to cut the workpiece along the central generatrix. Then, a micrometer with a sharp point attachment was used to measure the thickness of the workpiece. Figs. 6 and 7 indicate the comparison of sheet thickness distribution for numerical simulation and experiment in a developed length of the generatrix. A little deviation is observed at the contact area of the punch head and the workpiece.

4.5. Deformation history in simulation

Figs. 8 and 9 show the deformation history at different punch travel in the drawing and redrawing process. It was found that the blank was drawn smoothly into the die cavity by the cylindrical punch. Which establishes that the technology of generalized r_{min} can adequately trace the whole deformation history.

Table 2
The relation of CPU time versus venous integration schemes (unit: second)

Integration schemes	Drawing CPU time	Redrawing CPU time	Total CPU time
CST	1637.6	4616.0	6253.6
SM	2.385.8	3802.9	6187.7
FI	4310.5	7056.4	11366.9
SRI	4763.5	7147.2	11910.7

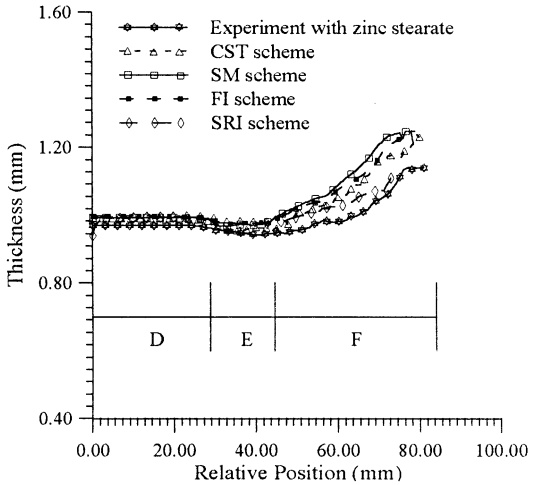

Fig. 7. Comparison of thickness for different integration schemes and experiment in the redrawing process.

5. Conclusion

Four different stiffness schemes, FI, SRI, RI and SM, are connected to the usual CST finite element program to investigate the computational efficiency of the sheet drawing and redrawing process. Comparison of the experiment and theoretical simulation results showed that the SM scheme and CST scheme had good agreement with the experiment in terms of punch load, thickness variation and deformation history. Moreover, under the consideration of sufficient accuracy, the CPU time for the SM scheme was less than that for the other schemes.

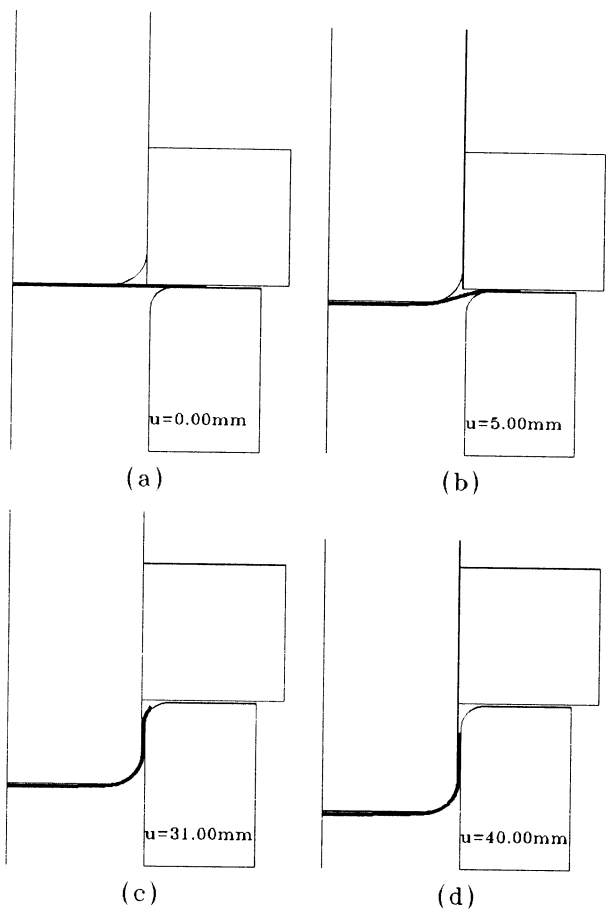

Fig. 8. The deformation history at different punch travels in the drawing process.

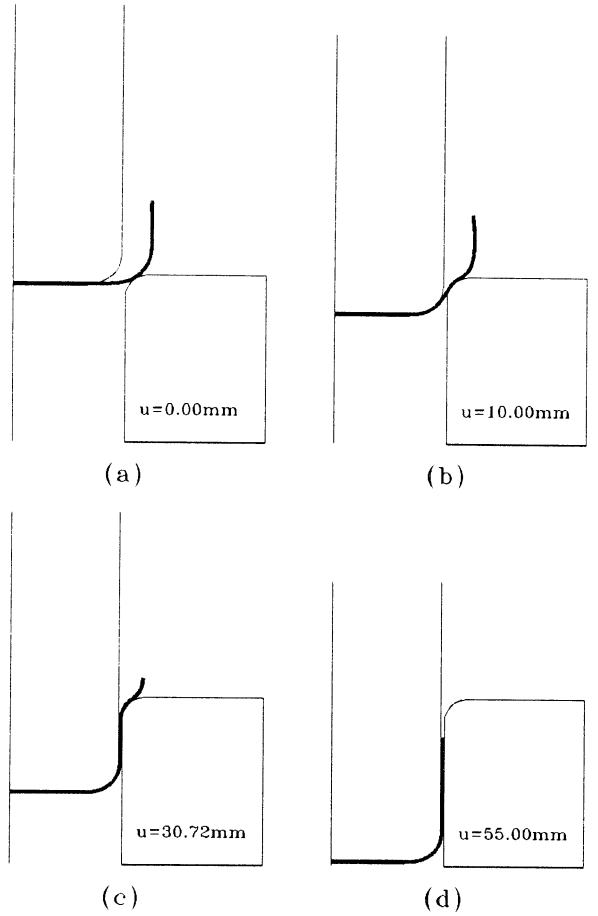

Fig. 9. The deformation history at different punch travels in the redrawing process.

Acknowledgements

The authors are grateful for the support from the National Science Council, Taiwan, Republic of China, under grant number NSC87-2212-E-011-015.

References

[1] S.Y. Chung, H.W. Swift, An Experimental Investigation of Re-Drawing of Cylindrical Cups, Process. Inst. Mech. Eng. UK (1952) 437–447.
[2] K. Nakamura, T. Nakagawa, Reverse deep drawing with hydraulic counter pressure using the peripheral pushing effect, Ann. CIRP 35 (1986) 73–176.

[3] M.H. Parsa, K. Yamaguchi, N. Takakura, S. Imatani, Consideration of the re-drawing of sheet metals based on finite-element simulation, J. Mater. Process. Technol. 47 (1994) 87–101.
[4] D.Y. Yang, J.B. Kim, D.W. Lee, Investigation into manufacturing of very long cups by hydromechanical deep drawing and ironing with controlled radial pressure, Ann. CIRP 44 (1995) 255–258.
[5] Y.H. Lu, C.L. Li, Y.M. Huang, Strategies for improving efficiency on axisymmetric sheet stretching process, J. Mater. Process. Technol. 63 (1997) 111–116.
[6] J.C. Nagtegall, D.M. Parks, J.R. Rice, On numerically accurate finite-element solutions in the fully plastic range, Comput. Methods Appl. Mech. Eng. 4 (1974) 153–177.
[7] D.V. Griffiths, G.G.W. Mustoe, Selective reduced integration of four-node plane element in closed form, J. Eng. Mech. 121 (1995) 725–729.
[8] T. Belytschko, J.S.-J. Ong, W.K. Liu, J.M. Kennedy, Hourglass control in linear and nonlinear problems, Comput. Methods Appl. Mech. Eng. 43 (1984) 251–276.
[9] T. Belytschko, C.S. Tsay, W.K. Liu, A stabilization matrix for the bilinear Mindlin plate element, Comput. Methods Appl. Mech. Eng. 29 (1981) 313–327.
[10] W.K. Liu, J.S.-J. Ong, R.A. Uras, Finite element stabilization matrices—a unification approach, Comput. Methods Appl. Mech. Eng. 53 (1985) 13–46.
[11] A. Makinouchi, H. Ogawa, Simulation of sheet bending processes by elastic-plastic finite-element method, Ann. CIRP 38 (1990) 279–282.
[12] A. Makinouchi, Y. Shirataki, S.D. Liu, Y. Nagai, Generalization of tool-work contact conditions for elasto-plastic analysis of forming process, Adv. Technol. Plast. 3 (1990) 1161–1166.